Simultaneous *SOHO* and *Yohkoh* Observations of a Small Solar Active Region

N. W. Griffiths[1], G. H. Fisher[1], D. T. Woods[1,2], L. W. Acton[3] and O. H. W. Siegmund[1]

[1]Space Sciences Laboratory, University of California, Berkeley, Berkeley, CA 94720-7450

[2]Lawrence Livermore National Laboratory, L-16, P.O. Box 808, Livermore, CA 94550

[3]Physics Department, Montana State University, Bozeman, MT 59717

Received _____; accepted _____

ABSTRACT

We present new results from observations of a small active region taken with the SUMER spectrograph and Extreme Ultraviolet Imaging Telescope (EIT) on *SOHO*, and the Soft X-ray Telescope (SXT) on *Yohkoh*. The SUMER study features line and continuum emission covering a wide range of temperatures, and includes the density-sensitive O IV] λ1400 multiplet. A more extensive analysis of quiet Sun data presented in a previous paper is also included. The presence of a power-law relationship between emission line power and electron density is confirmed, although the exponents in the active region are slightly higher than those found in the quiet Sun. These power-law relationships suggest that the volume filling factor decreases with density, and indicate possible differences between emitting material in active regions and the quiet Sun. We study active region emission measures from both the SUMER and SXT data sets. For the active region as a whole, SXT temperatures and emission measures appear to fit smoothly onto the emission measure distribution determined from cooler transition region and coronal lines in the SUMER spectra. We find no significant variation in the shape of the lower transition region emission measure distribution for different subregions of the data set. This reinforces the conclusion from the original quiet Sun paper that ensembles of "cool loops" are unlikely to be the source of this emission unless the structures are considerably smaller than the 1″ spatial resolution of SUMER.

Subject headings: sun: transition region — sun: UV radiation

1. Introduction

The 1995 launch of the *Solar and Heliospheric Observatory* (*SOHO*) started a new era in our understanding of the solar transition region. *SOHO* consists of 12 different instruments, including two spectrometers suitable for transition region investigations; the Coronal Diagnostic Spectrometer (CDS; Harrison et al. 1995) and Solar Ultraviolet Measurements of Emitted Radiation (SUMER; Wilhelm et al. 1995). These instruments have expanded upon earlier observations made with the Solar EUV Rocket Telescope and Spectrograph (SERTS; Neupert et al. 1992), S082-B EUV spectrograph (Bartoe et al. 1977), and High-Resolution Telescope Spectrograph (HRTS; Brueckner, Bartoe & VanHoosier 1977, Brueckner & Bartoe 1983). From its vantage point at L1, *SOHO* has enabled new studies of the transition region with unprecedented spatial, spectral, and temporal resolution.

In a recent paper Griffiths et al. (1999; hereafter Paper 1) discussed a 7 hour study of the quiet Sun made with the SUMER spectrograph on *SOHO*. SUMER includes a normal-incidence telescope and spectrometer, and can cover wavelengths from 330 to 1610Å depending on the spectral order and choice of detector. The spectral resolution is $\sim$ 43mÅ in first order and $\sim$ 22mÅ in second order, while the spatial resolution is $\sim 1''$. Paper 1 addressed several interesting features of the solar transition region, and the main conclusions can be summarised as follows: Images of the solar atmosphere from $\sim$ 6000 K to $\sim$ 2 MK indicate that the majority of the quiet Sun transition region emission arises from the physical interface between the chromosphere and corona, and not from so-called "unresolved fine structures" (UFS; Feldman 1983, 1987; Feldman & Laming 1994). The pixel brightness of these images shows a log-normal distribution, possibly indicative of small scale fragmentation. Simultaneous images in the density-sensitive O IV] λ1400 lines suggest a power-law relationship between emission line power and electron density, with an

exponent typically in the range ~ 0.3 to 1.0. In addition, the shape of the volume-integrated emission measure distribution is found to be largely invariant over many different intensity and spatial bins. This would appear to preclude an ensemble of "cool loops" (Antiochos & Noci 1986) as an explanation for the lower transition region structure, unless such loops are considerably shorter than the $\sim 1''$ spatial resolution of SUMER.

This new study is similar to that described in Paper 1, and includes an observation of a small active region. The relatively compact magnetic structures within active regions are very different from the longer magnetic loops associated with the quiet Sun, and we compare the active region results with a new analysis of the quiet Sun data. Observations from the *Yohkoh* Soft X-ray Telescope (SXT; Tsuneta et al. 1991) are also analysed, and intensity maps from the Extreme Ultraviolet Imaging Telescope (EIT; Delaboudinière et al. 1995) on *SOHO* are included.

2. Observations and Data Reduction

2.1. SUMER Data

A small active region about 35° directly north of disk center, with no known NOAA identification number, was observed by SUMER from UT 01:01 to UT 02:40 on 19 April 1997. This study includes lines from N II, N III, N IV, and N V formed over the temperature range $4.7 \lesssim \log T_e \lesssim 5.3$, and lines of O II, O III, O IV, and O V which are formed in a similar temperature range. The influence of transition region abundance uncertainties is minimised by confining our attention to lines from only two elements, although we acknowledge that the abundance of an individual element may vary as a function of temperature and height (Woods & Holzer 1991). A coronal line of Fe XII was also observed, and chromospheric information can be obtained from the C I continuum (taken next to the N V λ1238.8 line)

and the Lyman continuum (taken next to the O IV λ787.7 line). The observations were taken with the $0.3'' \times 120''$ aperture (the exact slit width is 0.278″) and the default detector at the time of the observations was detector B.

Since the SUMER slit-scanning mechanism was disabled during our observations, the data were taken with the slit fixed and the Sun rotating through our field of view. The emission lines of interest were split into four wavelength bands, and each band was subject to repeated 60 s exposures. A list of the observed lines in each band is given in Table 1. An average image of the Sun can be built up as it rotates through our slit position, but it should be noted that each band of emission lines corresponds to different regions of the solar surface (see §3 for a more detailed discussion). Consecutive exposures in each emission line are separated by about 6.7 minutes. During this time the Sun will have rotated by about 655 km at the position of the active region, corresonding to an angle of 0.9″ subtended at *SOHO*.

The flat-field correction was performed during the data reduction process, using a flat-field image created shortly after our observations. (Automatic inflight flat-fielding was possible but was not implemented). The optical design of SUMER introduces a slight distortion of the slit image, including wavelength dependent variations in the length of the slit on the detector. Since one end of the slit was obscured by a baffle behind the slit plane, the contraction of the slit image was estimated from the quiet Sun observations discussed in Paper 1 (where both ends of the slit were visible). The detector distortion effects were then corrected using an IDL code written by Giampiero Naletto, and our intensity arrays were normalized to a size of 70 pixels (i.e. $70''$) perpendicular to the dispersion axis. It is important to recognise that this corresponds to the size of the observed region projected onto the plane of the SUMER detector. Since the observed area was 35° north of disk center, our data covered an area that extended $85''$ in the north-south direction on the solar

surface. There were no significant projection factors in the east-west direction.

Each line profile was studied as a function of time, so that the position of the line on the detector and the level of the background could be accurately determined. Line intensities were found by summing the count rate per square arcsecond in a given emission feature, subtracting the local background, and applying the laboratory calibration of detector B corrected for the inflight decrease in sensitivity due to operations at low gain. Total emission line powers were determined by integrating the intensities over the area of the emitting region projected onto the plane of the sky, and multiplying by 4π steradians.

The quiet Sun observations presented in Paper 1 are also reanalysed in this study. We have recently discovered that the distortion removal routine used in the original analysis did not redistribute counts in an entirely even manner. The effect is only noticeable in the weakest lines. Integrated fluxes are essentially unchanged, but the density-sensitive O IV] λ1399.8/λ1401.2 line ratio is affected at low count rates (see §4.1). Our new reduction of the quiet Sun data is identical to that in Paper 1, with the exception that an updated distortion removal code (as used with the active region data) has been applied.

Statistical fluctuations can lead to negative values for background-subtracted fluxes in weak emission lines. We find that all negative pixels lie within 3σ of zero, where σ is the average Poisson noise on the background. Even though these pixels are statistically acceptable they can affect the determination of intensities over restricted regions of the data set (see §4.1).

2.2. *Yohkoh* SXT Data

The *Yohkoh* SXT (Tsuneta et al. 1991) is a grazing-incidence telescope covering the 3-45Å waveband. The instrument includes a CCD detector with 1024×1024 pixels, and

a set of broad-band filters on rotating filter wheels which can be used to measure the temperature and emission measure of the emitting plasma. In this paper we analyse full disk images taken at 5″ spatial resolution in the thin Al and AlMgMn-sandwich filters. The signal ratio from these filters is an indicator of typical active region temperatures ($\gtrsim 1$ MK), and standard SXT software has been used to determine temperatures and isothermal emission measure fits for the data (see §5).

3. Active Region Images

The nature of the SUMER observations makes it difficult to ascertain the exact structure of the observed region. A much clearer picture can be obtained from simultaneous images of the Sun taken with the *SOHO* EIT. The longitudinal positions of the SUMER exposures relative to the complete active region (imaged in the EIT Fe XII λ195 bandpass) are shown in Figure 1. It appears that the SUMER exposures recorded emission from one side of an arcade of coronal loops. A comparison of the Fe XII intensity patterns in SUMER and EIT suggests that the two instruments were very closely aligned during the observation sequence. Figure 1 also indicates the position of the active region on the solar disk at the time of the observations.

SUMER intensity maps are shown in Figure 2, which includes images made in the transition region lines, the coronal line of Fe XII, and the two chromospheric continuum emissions. The C I and Lyman continua are formed at about 6000 K and 8000 K respectively ($\sim$ 1000 km and $\sim$ 2000 km above $\tau_{5000} = 1$) in the solar atmosphere (Vernazza, Avrett, & Loeser 1973). Although the intensity maps are displayed as arrays of 15×70 elements (15 exposures, each of height 70″), the observed area actually extends about 13″ in the east-west direction. In addition, since the observed area was 35° north of disk center, our data covered an area that extended $85''$ in the north-south direction on the solar surface.

Note that only the central area of these images actually covers the loop structures of the active region. Although these observations will be described as the "active region data", only a restricted portion of the data can be considered to arise from the (relatively weak) active region. This important point will be addressed again in §4.3.

As mentioned in §2.1, this study is made up of multiple exposures in four separate wavelength bands. Because of solar rotation, observations in different bands cover slightly different regions of the solar surface. The overlap between Bands 1 and 2 is considerable (about 60% of the area covered by each exposure). There is a similar overlap between Bands 3 and 4. However, the common region between Bands 2 and 3 is only about 30%, and there is no overlap between Band 1 and Bands 3 or 4. In principle this could restrict the data analysis, but a closer consideration of the images suggests otherwise. Figure 3 shows the autocorrelation coefficients along the slit for three individual exposures in various emission lines. Perpendicular to the dispersion axis the coefficients appear to decrease by less than 10% over $1''$. Since the midpoints of the regions covered by bands 1 and 4 are separated by only $\sim 0.6''$, it would appear that emission line fluxes from corresponding exposures in different bands can be compared with some confidence.

Figure 4 shows coronal intensity maps from the thin Al and AlMgMn-sandwich filters on the *Yohkoh* SXT. Note that the harder emission in the AlMgMn filter occurs higher up in the active region structure. Figure 4 also indicates the sections of these images which overlap with the SUMER observations.

4. Line Emission and Electron Density

4.1. Intensity Distributions

Figure 5 shows intensity distributions for the different SUMER data sets. The histograms show the variation in counts per pixel for an integration time of 60s. Vertical dotted lines identify count rates at which the signal to noise ratio is equal to 3, and therefore indicate the range over which we can have most confidence in the shape of the distribution.

For quiet Sun data in which the signal to noise is greater than 3 the pixel brightness appears to be lognormally distributed. This confirms the result from Paper 1, to which the reader is referred for a more detailed discussion. The active region count rates are too low for the true intensity distributions to be determined, although the results for the strongest lines (e.g. O IV) suggest a similar pattern to the quiet Sun.

4.2. Power-Law Relationships

In Paper 1 it was concluded that the total power in quiet Sun transition region emission lines can be expressed as

$$P = C\, N_e^{\nu}, \tag{1}$$

where C and ν are constant for a given line, and N_e is the electron density determined from the O IV] λ1399.8/λ1401.2 line ratio. Over quiet Sun densities of $9 \lesssim \log N_e \lesssim 10$, ν was found to be in the range ~ 0.3 to 1.0. As mentioned in §2.1, the detector distortion removal routine used in Paper 1 redistributed counts in a slightly uneven manner. The relative redistribution of counts in the O IV] λ1399.8 and λ1401.2 lines meant that the density of the dimmest regions, and therefore the value of ν, were both overestimated.

In this paper an improved distortion removal routine has been used, and a new analysis

of the quiet Sun images is now compared with a similar study of the active region data. The O IV] λ1399.8/λ1401.2 ratio and the results of Cook et al. (1995) are used to determine the electron density. The quiet Sun images (each with 18000 pixels) are sorted into ten intensity bins, while the smaller active region images (each with 1050 pixels) are arranged into five intensity bins. The total emitted power and average electron density are computed for every intensity bin in each emission line. Bins with anomalously low O IV] line ratios are set to the low-density limit of $\log N_e = 8.0$. It should be emphasised that the electron density is determined at the formation temperature of O IV ($\log T_e \sim 5.25$). However, since the pressure through the transition region and coronal plasma in a magnetic loop is approximately constant (see e.g. O'Shea, Doyle, & Keenan 1998) the value of ν is largely independent of the temperature at which N_e is determined. If we had another reliable density diagnostic this statement could be tested.

The results for both data sets are shown in Figure 6, with the quiet Sun emission scaled to the area of the active region data bins (71.3 arcsec^2). It is interesting to note that the surface fluxes from the brightest parts of the quiet Sun are comparable to the surface fluxes from the loop structures in our weak active region. The best fit to each set of data points is shown as a dashed line, and details of the fits are given in Table 2. These fits ignore any bins near the low-density limit and any bins that are *dominated* by negative count-rate pixels (which may include up to 20% of the field of view). Note that large uncertainties on $\log C$ simply reflect the level of uncertainty in ν. With the exception of the weak N II line, we find that the ν values for the quiet Sun are well constrained and lie between 0.3 and 0.6. The average value is around 0.4, somewhat lower than that found in Paper I.

4.3. Discussion

The power-law relationships have interesting implications for the volume of the emitting plasmas. The power in an emission line can be expressed as

$$P = \int G(T_e) N_e N_H dV = \int X G(T_e) N_e^2 dV, \tag{2}$$

where $G(T_e)$ is the line emissivity calculated in the coronal approximation and $X = N_H/N_e$. In the simplest case of a volume V of plasma at constant density and temperature, equation (2) can be written as

$$P = X G(T_e) N_e^2 V. \tag{3}$$

If a power-law relationship such as equation (1) applies, the density dependence of the emitting volume is given by

$$V = \frac{C}{X G(T_e)} N_e^{\nu-2}. \tag{4}$$

The precise relationship between V and N_e will be slightly different from equation (4) because each emission line is formed over a range of temperatures (typically $\Delta \log T_e = 0.3$) and the plasma responsible for this emission will include some density variations. But as long as ν is clearly less than 2 the emitting volume will decrease with density. What does this mean in physical terms? The pixels in each intensity bin are spread across the field of view, but we can assume as a first approximation that the line-of-sight plasma column in every pixel in each intensity bin is similar. The flux from each emission line is then presumed to come from a layer of plasma within the combined area, and it is the volume of this layer that must decrease with density.

Figure 6 and Table 2 indicate two main differences between the data sets. Namely, it is clear that the active region has higher electron densities and larger ν values than the quiet Sun. The active region densities cover the range $10 \lesssim \log N_e \lesssim 11$, while ν typically varies from 0.8 to 1.5. Even higher values of ν are indicated for the N II λ776.0, N III λ764.4,

O V λ760.2 and N V $\lambda\lambda$1238.8, 1240.8 lines. However, the N III and O V values are highly uncertain and the Li-sequence N V lines are known to exhibit other anomalous behaviour (see §5 and Paper 1). The N II value appears to be well constrained, but the weak nature of the line suggests that this may be coincidental. The quiet Sun data covers densities of $9 \lesssim \log N_e \lesssim 10$, with ν typically between 0.3 and 0.6. We see that regions of the quiet Sun and active region data sets which have similar surface fluxes may have electron densities that differ by up to an order of magnitude. Equation (3) then suggests that the emitting volume per unit surface area is up to a factor of 100 less in the active region data than it is in the quiet Sun. This is rather surprising, but it is worth noting that Dere et al. (1987) report area filling factors spanning three orders of magnitude in the transition region.

Our results may indicate fundamental differences between the two data sets, but it is essential to determine the importance of instrumental configurations and operations. Specifically, could changes in the number of counts in each intensity bin lead to systematic variations in the power-law relationships? There are three main factors affecting the total counts: the intrinsic plasma brightness, the slit size, and the number of exposures. The quiet Sun data comprises 60 exposures, each of size $1'' \times 300''$. The active region data includes 15 exposures, each of which covers $0.28'' \times 85''$ on the solar surface. Figure 6 suggests that there is a similar range of transition region surface fluxes in both data sets. To investigate the importance of instrumental factors such as slit size and number of exposures, $15'' \times 85''$ subregions of the quiet Sun O IV λ787.7 and N IV λ765.1 data sets have been reanalysed. The complete $60'' \times 300''$ data set was divided into 42 subregions, each of which overlaps half the adjacent subregion in both the north-south and east-west directions. The power-law relationship was determined over five intensity bins for each subregion. The O IV λ787.7, N IV λ765.1, O IV] λ1399.8 and O IV] λ1401.2 data sets were then "degraded" to simulate the counting statistics in the active region data. This involved multiplying the number of counts per pixel by a factor of 0.28 (to account for the difference in slit widths),

and folding in random Poisson noise consistent with the lower count rate. Values of ν were then determined for the "degraded" data in each subregion.

As shown in Figure 7, we find a range of ν values from the 42 subregions. There is no clear evidence for systematic variations in the distribution of ν between the original and "degraded" data sets, suggesting that the change in slit width is not critical. However, the variation in ν suggests that the power-law relationship may depend upon the particular region over which it is calculated. Even though the distributions peak around the values for the complete quiet Sun data sets ($\nu \sim 0.4$), there exist $15'' \times 85''$ subregions in which ν is similar to the value for the active region data. But are there subregions in which both ν and the electron density are similar to the active region results? Figure 8 compares ν in a given subregion with $\log N_e$ for intensity bins in that subregion. There is evidence for a decrease in the value of ν at higher densities, and it would seem that the active region results are not reproduced by any subregion of our quiet Sun image.

These tests seem to confirm the differences between quiet Sun and active region data. This is an intriguing result, not least because much of the active region data is visually similar to the quiet Sun. Only the highest intensity bin actually covers the bright loop structures, but typically all five intensity bins appear consistent with a single power-law relationship. This could indicate that areas surrounding active regions are untypical of the quiet Sun. The limited data discussed here cannot be used to draw global conclusions about the solar transition region, and further work is clearly required.

5. Emission Measure Distributions

The following analysis is similar to that given in §6 of Paper 1, to which the reader is referred for a more detailed discussion of emission measure definitions. Here we work in

terms of EM(0.3), the emission measure integrated over $\Delta \log T_e = 0.3$. If T_f is the peak formation temperature for a given line then

$$\mathrm{EM}(0.3)_{T_f} = \int_{\log T_f - 0.15}^{\log T_f + 0.15} N_e N_H \, dV. \tag{5}$$

Note that EM(0.3) can be related to the differential emission measure (see equation [5] of Paper 1). Average empirical emission measure distributions have been determined using the method described in Griffiths & Jordan (1998). The N V lines are not included in the calculation of average EM(0.3) distributions. These lines are significantly brighter than expected, probably due to dynamical processes affecting the ionization equilibrium (e.g. Hansteen 1993 - see Paper 1 for discussion). All the atomic physics used to investigate the emission measure distributions have been taken from the CHIANTI database (Dere et al. 1997), and the solar photospheric abundances of Anders & Grevesse (1989) have been adopted. There appear to be some small systematic differences between the emission measures derived from the N and O lines, possibly due to abundance effects. When deriving average distributions more weight has been placed on the O lines since these generally have significantly higher count rates. Using the emission lines in our data set, the average distribution is well constrained over the temperature range $4.4 \lesssim \log T_e \lesssim 5.5$.

Figure 9 compares emission measure distributions from three separate subregions of the data set, while Figure 10 shows emission measures averaged over the entire data set. Average distributions are shown, along with emission measure loci for the individual lines. These loci are calculated assuming that all the emission in a given line is formed at one single temperature, and they place an upper limit on the emission measure at any temperature. Two different loci are shown for the Fe XII λ1242.0 line. The upper locus is calculated for a photospheric Fe abundance. The lower locus assumes that the Fe abundance is enhanced over the O and N abundances by a factor of ~ 4.5, typical of the first ionization potential (FIP) effect (Grevesse & Anders 1991). It is not known whether

possible FIP effect abundance variations are caused by enhancement of low FIP elements (e.g. Fe) or depletion of high FIP elements (e.g. O and N). For ease of display our results are plotted assuming the Fe abundance is enhanced, but this may not be the case.

The average EM(0.3) distributions from the three subregions in Figure 9 have remarkably consistent shapes. Only the central region (middle panel of Figure 9) is associated with the loop structures, while the two other subregions cover much dimmer material. Similar consistency was noted in Paper 1 for the average distributions from various spatial and intensity bins of the quiet Sun. It was argued that the emission measure distribution below $\log T_e \sim 5.2$ was therefore unlikely to be due to the relative populations of various types of "cool loops", unless the spatial extent of such structures were subresolution (i.e. $< 1''$). The current analysis clearly supports this conclusion.

The emission measure distribution is less well constrained above $\log T_e = 5.5$. Assuming a curve of the form $\mathrm{EM}(0.3) \sim T_e^{\alpha}$, the Fe XII line can be used to estimate the "gradient" α between $\log T_e = 5.3$ and $\log T_e = 6.2$. Using photospheric abundances, α values of 3.1, 2.9, and 2.9 are found for the upper, middle and lower subregions respectively in Figure 9. Adopting FIP effect abundances, α changes to 2.4, 2.1, and 2.2, respectively. These values of α are systematically higher than the corresponding values found in Paper 1, in line with previous comparisons of the quiet Sun and active regions (e.g. Raymond & Doyle 1981, and references therein).

Figures 9 and 10 also include emission measures calculated from SXT count rates. Emission measure "loci" have been determined for data from the thin Al and AlMgMn filters. These emission measures are likely to be higher than EM(0.3) values since the SXT filters are sensitive to an extended range of plasma temperatures ($\Delta \log T_e \gg 0.3$). The SXT curves agree reasonably well with the Fe XII loci, and they certainly indicate a decrease in emission measure at the highest temperatures. The intersection of the thin

Al and AlMgMn curves is equivalent to the results of an isothermal emission measure fit. Although isothermal models are approximations to real coronal plasmas, they do offer clues to the nature of the emitting material. The position of the SXT isothermal fit in the top panel of Figure 9 may be evidence for small amounts of hard emission near the loop apex (as mentioned in §3). Furthermore, Figure 10 suggests that SXT temperatures and emission measures for small active regions fit smoothly onto the emission measure distribution determined from transition region and low coronal emission lines.

6. Conclusions

The data analysis presented here supports many of the conclusions from Paper 1. The presence of a power-law relationship between emission line power and electron density has been confirmed, suggesting that the emitting volume *decreases* with density. The volume filling factor is therefore smaller in the bright regions. In addition, a study of emission measures from different subregions of the active region data has provided further evidence against populations of "cool loops" explaining the lower transition region emission measure distribution.

A comparison of the active region and quiet Sun data also reveals several new results. The brightest parts of the quiet Sun have comparable surface fluxes to the active region loop structures, and we see a similar range of surface fluxes in both data sets despite the difference in electron densities. The lower volume filling factor inferred for the active region is rather unexpected, if only because the dimmer parts of this data set look (at least superficially) like the quiet Sun. It is possible that areas around active regions have lower filling factors than the average quiet Sun, and we emphasise that there are no subregions of our quiet Sun data in which both ν and $\log N_e$ are similar to the values in the active region. This study cannot determine the global pattern of filling factors and power-law

relationships, but it has raised enough interesting questions to demonstrate the need for further studies of transition region structure.

The authors wish to thank Jim McTiernan for his assistance with *Yohkoh* SXT data analysis. This research was supported by NASA grant NAG5-7351.

REFERENCES

Anders, E., & Grevesse, N. 1989, Geochim. Cosmochim. Acta, 53, 197

Antiochos, S. K., & Noci, G. 1986, ApJ, 301, 440

Bartoe, J.-D. F., Brueckner, G. E., Purcell, J. D., & Tousey, R. 1977, Appl. Opt., 16, 879

Brueckner, G. E., & Bartoe, J.-D. F., 1983, ApJ, 272, 329

Brueckner, G. E., Bartoe, J.-D. F., & VanHoosier, M. E. 1977, in Proceedings of the OSO-8 Workshop, ed. E. Hansen & S. Schaffner (Boulder:University of Colorado), 380

Cook, J. W., Keenan, F. P., Dufton, P. L., Kingston, A. E., Pradhan, A. K., Zhang, H. L., Doyle, J. G., & Hayes, M. A. 1995, ApJ, 444, 936

Delaboudinière, J. -P., et al. 1995, Sol. Phys., 162, 291

Dere, K. P., Bartoe, J.-D. F., Brueckner, G. E., Cook, J. W., & Socker, D. G. 1987, Sol. Phys., 114, 223

Dere, K. P., Landi, E., Mason, H. E., Monsignori Fossi, B. C., & Young, P. R. 1997, A&AS, 125, 149

Feldman, U. 1983, ApJ, 275, 367

Feldman, U. 1987, ApJ, 320, 426

Feldman, U., & Laming, J. M. 1994, ApJ, 434, 370

Grevesse, N., & Anders E. 1991, in Solar Interior and Atmosphere, ed. A. N. Cox, W. C. Livingston & M. S. Matthews (Tucson:University of Arizona), 1227

Griffiths, N. W., & Jordan, C. 1998, ApJ, 497, 883

Griffiths, N. W., Fisher, G. H., Woods, D. T., & Siegmund, O. H. W. 1999, ApJ, 512, 992 (Paper 1)

Hansteen, V., 1993, ApJ, 402, 741

Harrison, R. A., et al. 1995, Sol. Phys., 162, 233

Neupert, W. M., Epstein, G. L., Thomas, R. J., & Thompson, W. T. 1992, Sol. Phys., 137, 87

O'Shea, E., Doyle, J. G., & Keenan, F. P. 1998, A&A, 338, 1102

Raymond, J. C., & Doyle, J. G. 1981, ApJ, 247, 686

Tsuneta, S., Acton, L., Bruner, M., Lemen, J., Brown, W., Caravalho, R., Catura, R., Freeland, S., Jurcevich, B., & Owens, J. 1991, Sol. Phys., 136, 37

Vernazza, J. E., Avrett, E. H., & Loeser, R. 1973, ApJ, 184, 605

Wilhelm, K., et al. 1995, Sol. Phys., 162, 189

Woods, D. T., & Holzer, T. E. 1991, ApJ, 375, 800

Table 1. SUMER Observations - Study Bands and Emission Lines

Band 1		Band 2		Band 3		Band 4	
Ion	λ (Å)	Ion	λ (Å)	Ion	λ (Å)	Ion	λ (Å)
O V	760.228	O II	833.332	N V	1238.821	O IV]	1399.774
O V	760.445	O II	834.462	N V	1242.804	O IV]	1401.156
N III	764.357	O III	833.742	Fe XII	1242.010	O IV][a]	1404.812
N IV	765.143					O IV][b]	1407.386
N II	775.965						
O IV	787.711						

[a]Blended with S IV λ1404.770.

[b]Blended with O III λ703.850 in second order.

Table 2. Fit Parameters for Emission Line Power $P = C\,N_e^{\nu}$

			Active Region		Quiet Sun	
Ion	$\log T_e^a$	λ (Å)	ν	$\log C^b$	ν	$\log C^b$
N II	4.7	776.0	3.1±0.3	-13.0±3.7	0.8±0.4	11.3±3.7
N III	5.0	764.4	3.5±5.2	-17.6±55.0	0.4±0.1	15.3±1.1
N IV	5.2	765.1	1.1±0.1	9.0±0.4	0.4±0.2	16.4±1.9
N V	5.3	1238.8	1.9±0.3	0.6±3.0	0.6±0.1	15.0±1.2
N V	5.3	1242.8	1.9±0.3	0.1±3.6	0.4±0.1	16.1±0.5
O II	4.8	833.3	1.4±0.3	4.9±3.6	0.3±0.1	16.7±1.2
O II	4.8	834.5	1.2±0.5	6.9±5.3	0.3±0.1	16.9±0.9
O III	5.0	833.7	1.1±0.3	8.6±3.2	0.4±0.1	16.0±0.7
O IV	5.25	787.7	0.8±0.3	12.5±3.5	0.4±0.1	16.4±1.2
O V	5.4	760.2	3.4±3.9	-16.8±41.4	0.4±0.2	15.5±1.6
O V	5.4	760.4	1.4±0.6	5.3±5.8	0.5±0.1	15.5±1.3
Fe XII	6.2	1242.0	0.9±0.6	10.6±5.8	0.2±0.1	17.8±0.3

[a]Temperature at which line emission is maximum.

[b]Calculated for 71.3 arcsec^2 on the solar surface.

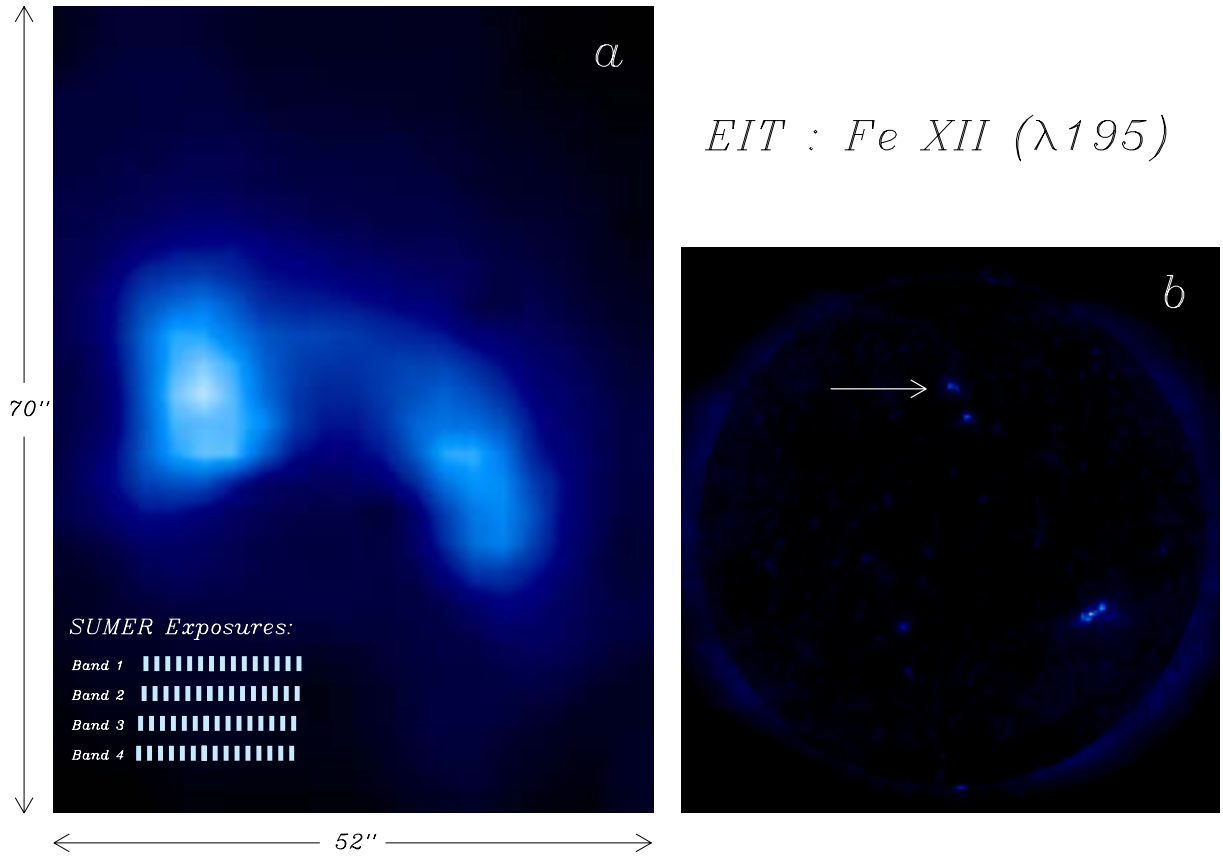

Fig. 1.— Images of the active region taken in the EIT Fe XII λ195 channel. (a) A close-up image covering 52″ × 70″ in the plane of the EIT detector, and aligned with the SUMER images in the north-south direction. Longitudinal positions of the SUMER exposures in each observation band are also shown. The width of the bars in the east-west direction indicates the actual extent of each exposure. (b) A full disk image in the EIT Fe XII λ195 channel. The arrow indicates the active region under study.

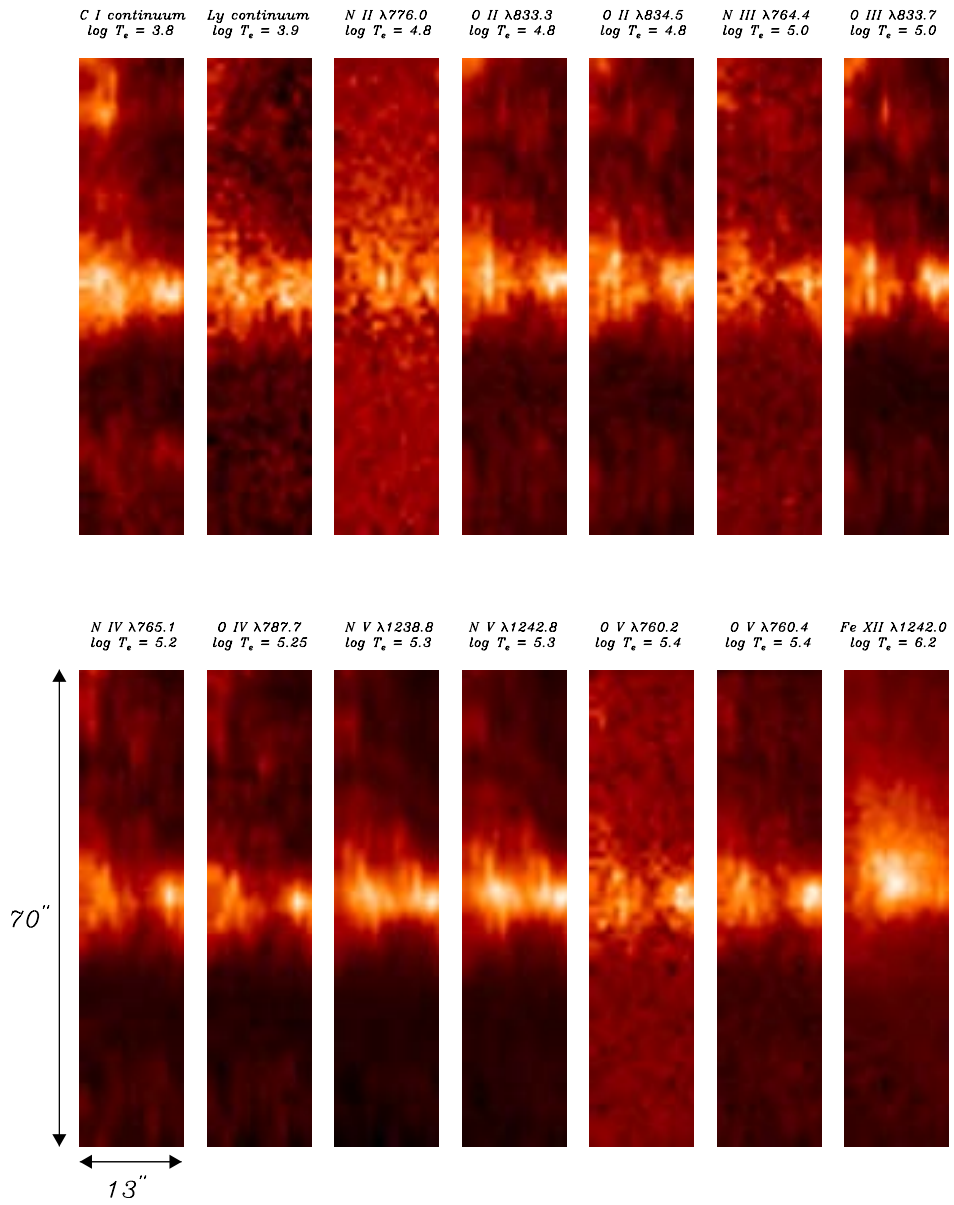

Fig. 2.— SUMER intensity maps. These images show the projection of the active region onto the plane of the SUMER detector. The observation consists of 15 exposures, encompassing an area that extends about 13″ in the east-west direction. Since the active region is about 35° above disk center, the observed region actually extends about 85″ in the north-south direction on the solar surface.

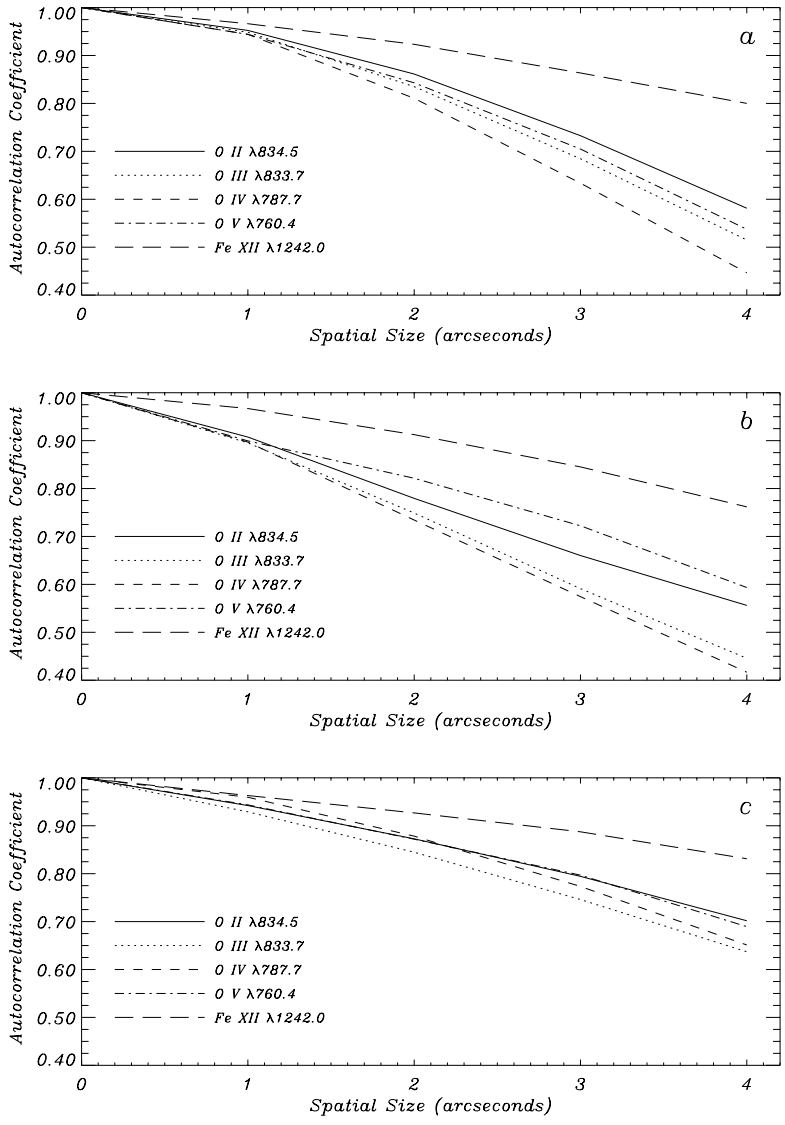

Fig. 3.— (a) Autocorrelation coefficients along the SUMER slit for the third exposure. Note that 1 pixel $\simeq 1''$ at L1. (b) Same as (a), but for the eighth exposure. (c) Same as (a), but for the thirteenth exposure.

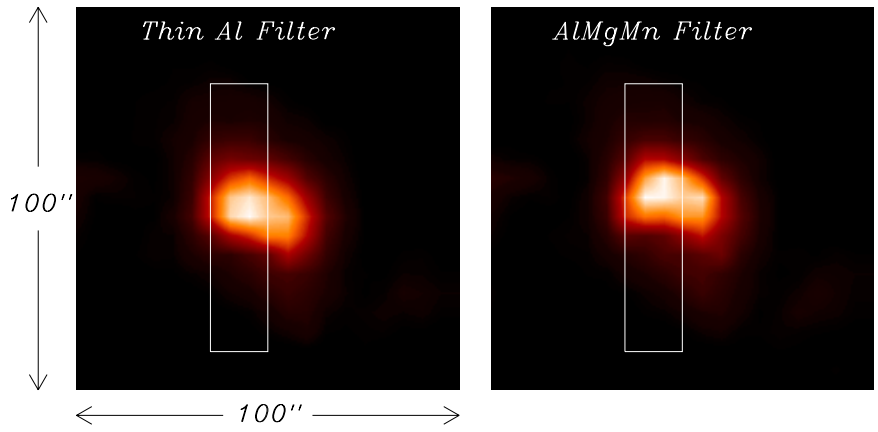

Fig. 4.— *Yohkoh* SXT intensity maps in the thin Al and AlMgMn filters projected onto the plane of the detector. The rectangular boxes indicate the region used for comparison with the SUMER data.

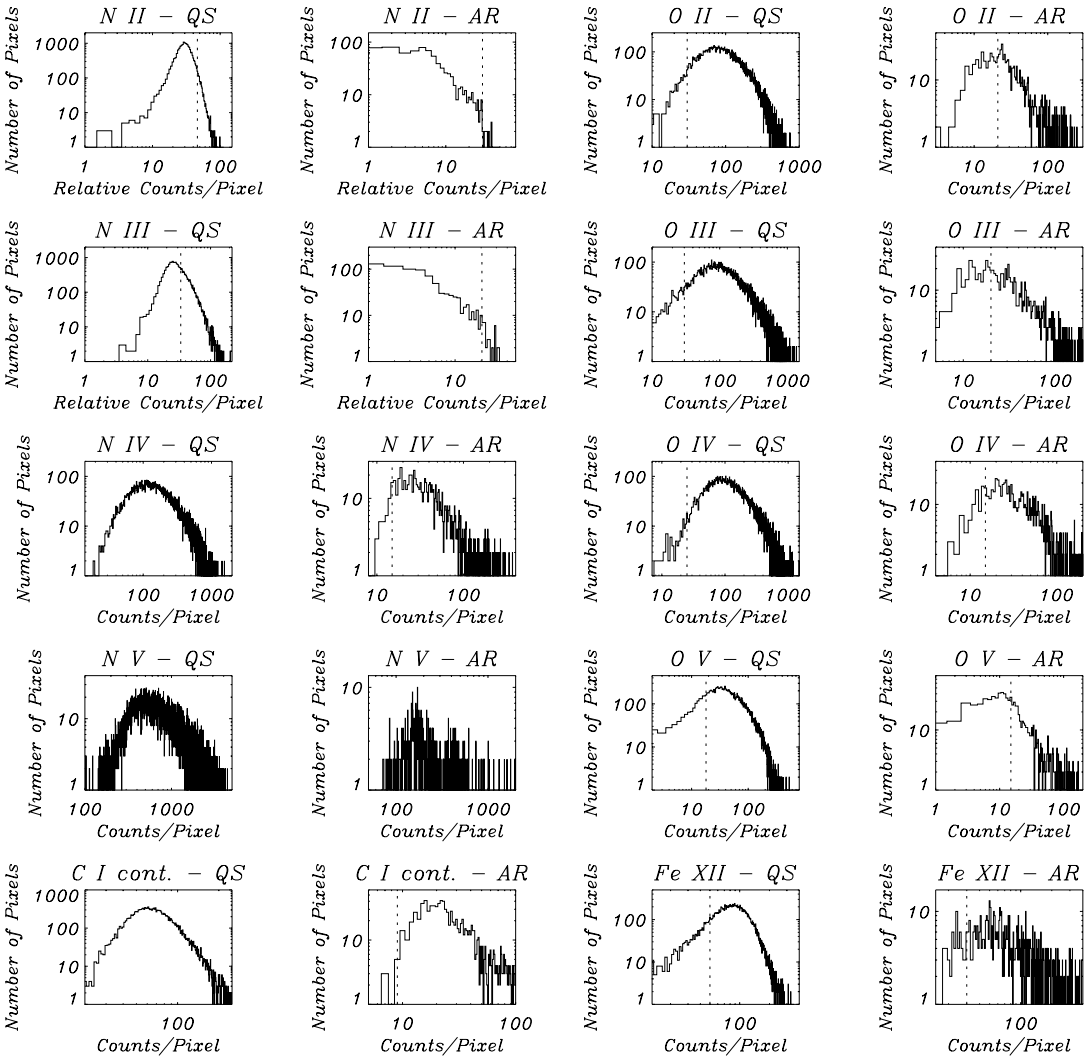

Fig. 5.— Intensity distributions for the two data sets. Dotted lines indicate thresholds at which S/N=3. (In the strongest emissions all pixels lie above this threshold). In most plots the x-axis shows the actual number of counts per pixel, but the weak N II and N III data sets include larger numbers of negative pixels (see §2.1). We note that the counts per pixel in N II ranges from -26.1 to 87.6 in the quiet Sun, and from -14.8 to 50.2 in the active region data. N III ranges from -16.6 to 223.6 in the quiet Sun, and from -5.4 to 43.0 in the active region. Since the binsize=1 in all plots, the possible count rate offsets in the weak lines may distort the shape of the intensity distributions.

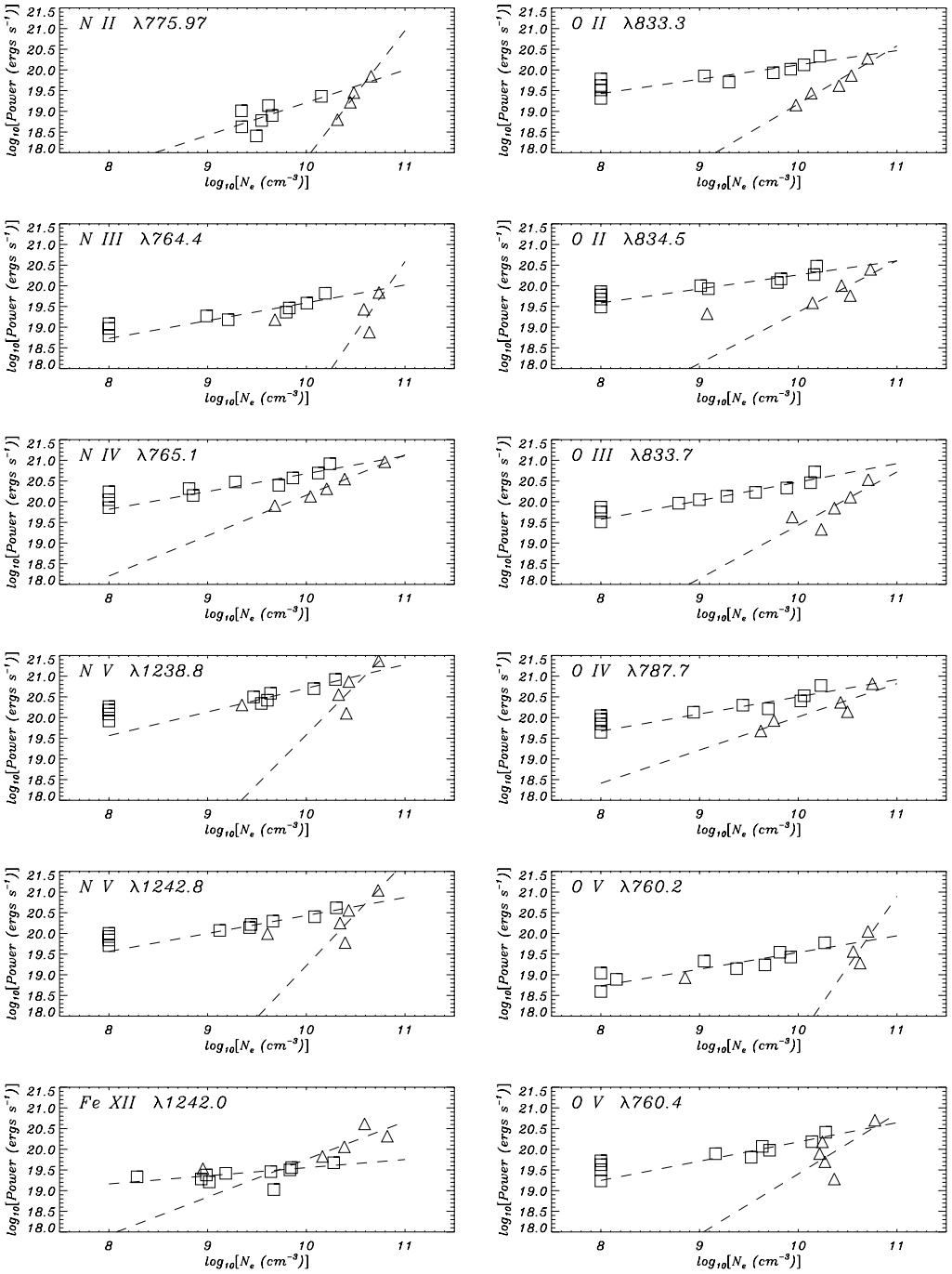

Fig. 6.— A comparison of total emission line power with electron density (derived from the O IV λ1399.8/λ1401.2 line ratio). Active region data (triangles) include five intensity bins in each emission line. Quiet Sun data (squares) use ten intensity bins. Dashed lines show the best fits to the data points. Details of these fits are given in Table 2.

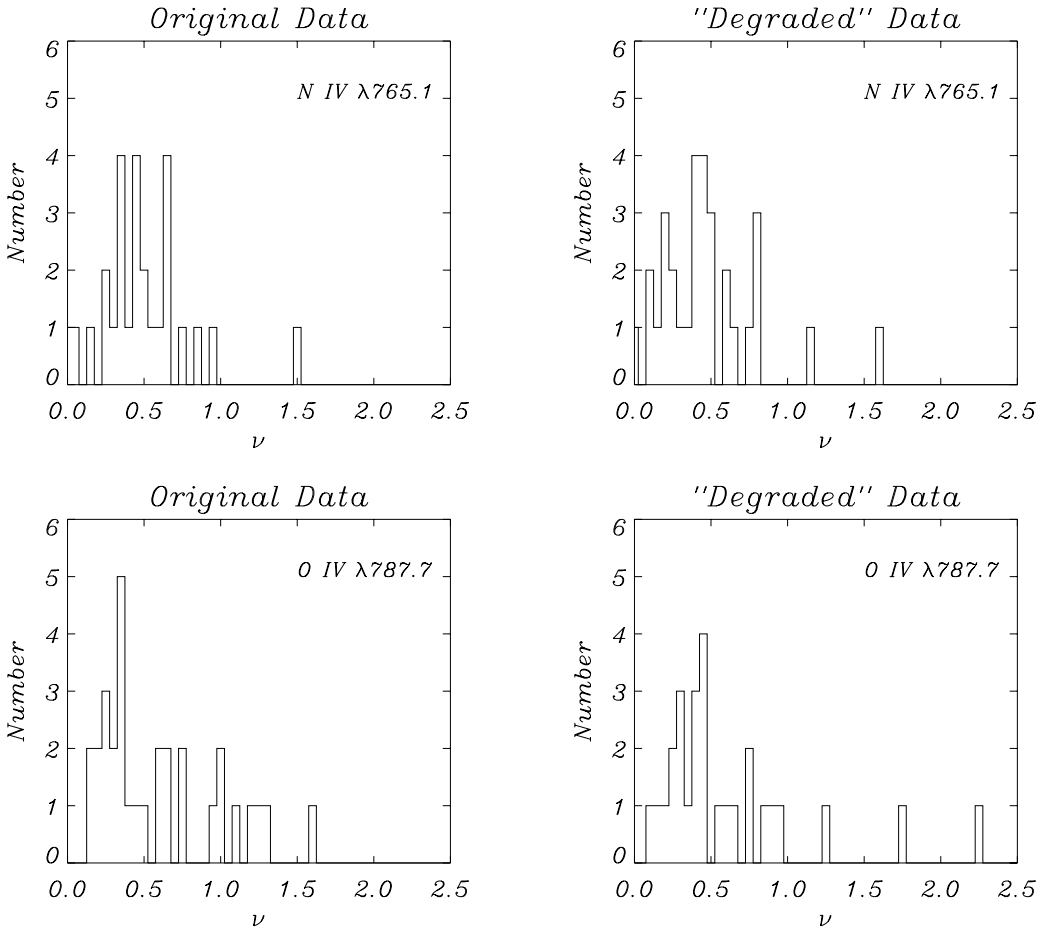

Fig. 7.— Histograms showing the distribution of ν in $15'' \times 85''$ rectangular portions of the N IV λ765.1 and O IV λ787.7 quiet Sun data. Results are shown for both the original data and "degraded" data. The count rates in the "degraded" data have been muliplied by a factor of 0.28 and varied with random Poisson noise to simulate the counting statistics in the active region observations.

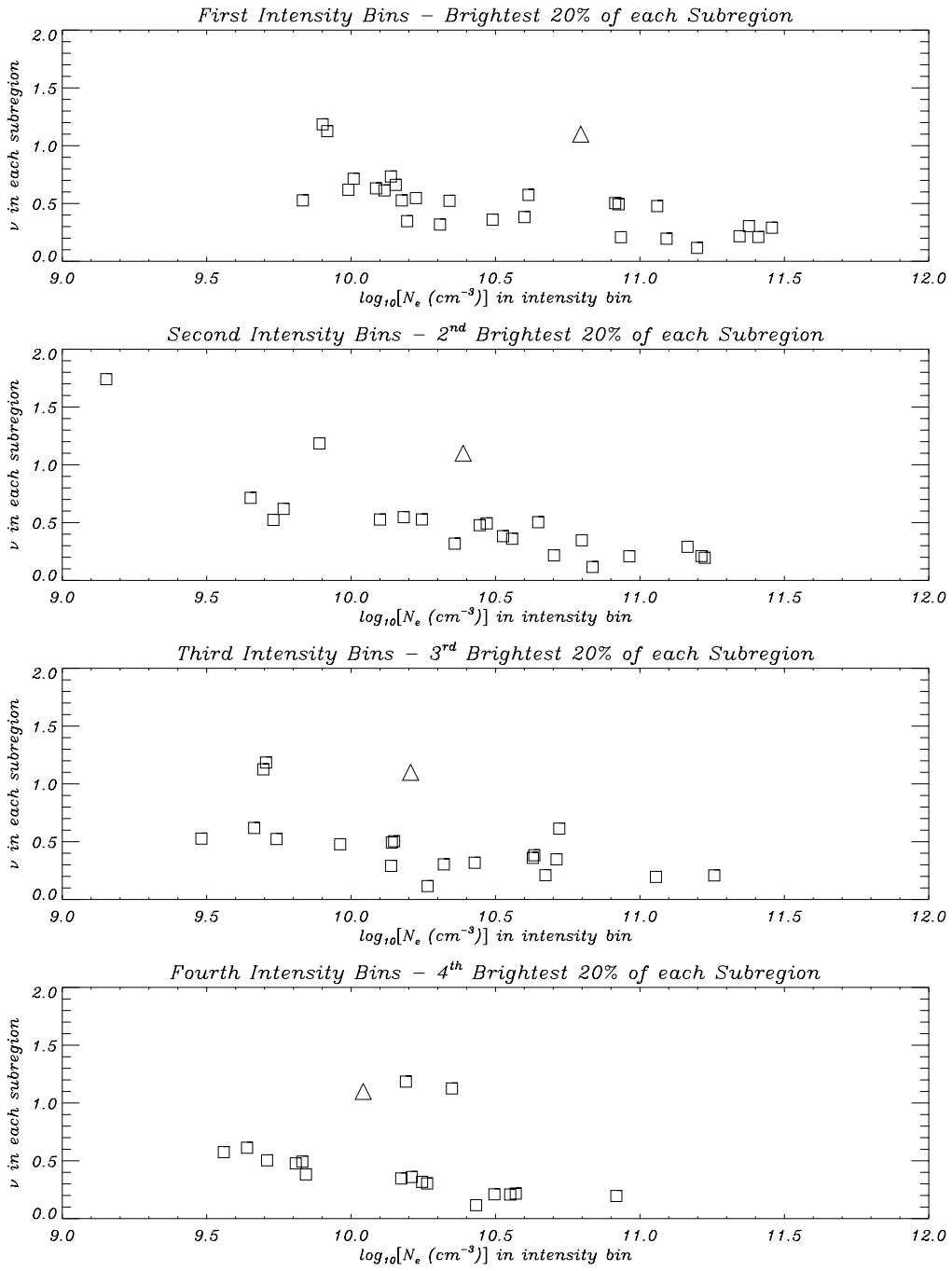

Fig. 8.— A comparison of ν values and electron densities in $15'' \times 85''$ subregions of "degraded" quiet Sun data (squares) and the active region data (triangles). The panels show results for corresponding intensity bins in the different subregions.

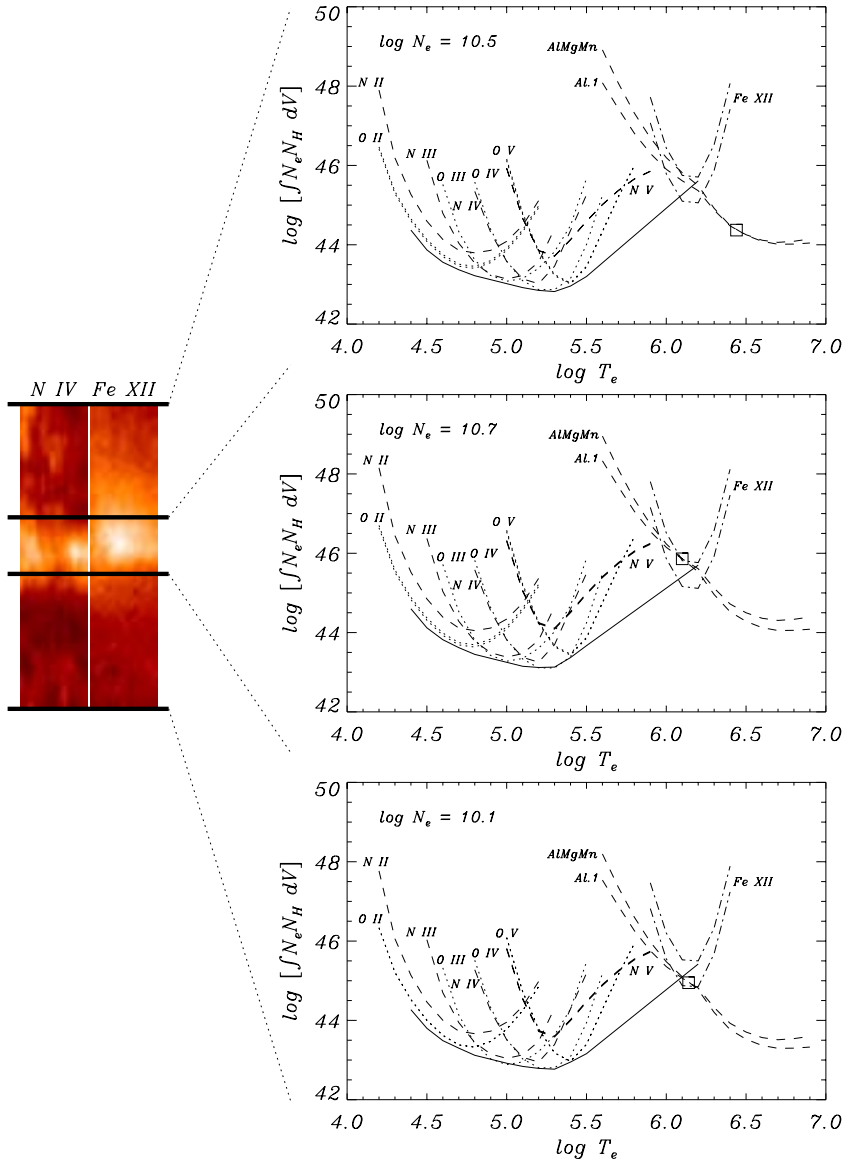

Fig. 9.— Emission measure distributions from three subregions of the active region data set. Average EM(0.3) distributions are shown as solid curves for $4.4 \leq \log T_e \leq 5.5$. Over the range $5.5 < \log T_e \leq 6.2$ the average distribution is poorly constrained, but estimates are shown. Emission measure loci are shown as short-dash curves (nitrogen lines), dotted curves (oxygen lines), dash-dot curves (Fe XII) and long-dash curves (*Yohkoh* SXT filters). The average electron density over each subregion is also noted. The squares indicate isothermal emission measure fits derived from the SXT filter count rates.

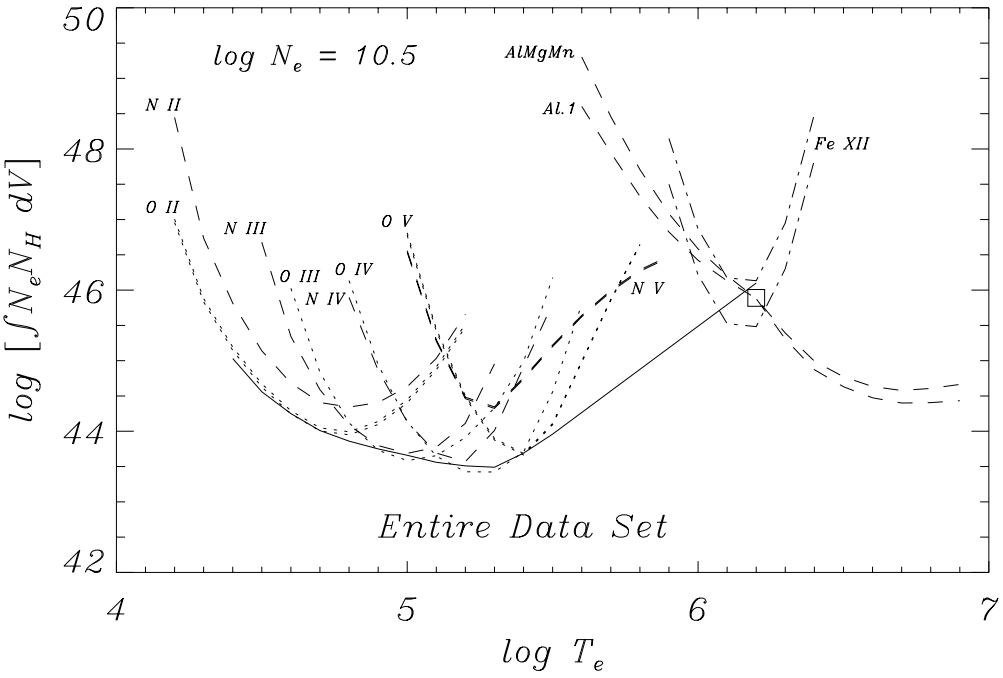

Fig. 10.— As Fig. 9, but for the entire data set.